HiSST: International Conference on
High-Speed Vehicle Science Technology

26–29 November 2018, Moscow, Russia

Experimental and Numerical Achievements in High Temperature Management for Hypersonic Flight

Hannah Böhrk[1], Tina Stäbler[2], Christian Dittert[2], Isil Sakraker[2], Daniel Prokein[3]

Keywords: *high temperature, structure, monitoring, transpiration cooling, imaging*

1. Introduction

Thermal protection of flight vehicles in hypersonic flight is extremely challenging due to the severe aerodynamic heating of external structures. Slender geometries such as a sharp leading edge of the forebody or the wing of low drag vehicles are especially affected by high heat loads. With respect to **reusability and availability over the designed life time** it is therefore necessary to employ active cooling methods such as **transpiration cooling**. In this context, porous ceramic matrix composites (CMC) in combination with transpiration cooling become interesting and have recently been investigated with increasing efforts. Transpiration cooling as an active cooling technique is based on two mechanisms: First, the exchange of energy while the coolant gas is flowing through the hot porous material and second, the injection of cool fluid into the boundary layer which decreases the effective heat load. Other aerospace solutions incorporate passive cooling with **ablators**. The involved physics for both processes are complex. This is especially true for materials such as the ceramic matrix composites (CMC) and recessing ablators developed by DLR Stuttgart which, on the other hand, exhibit promising properties for high-temperature aerospace applications.

High Temperature Management therefore, focuses on the development of required **numerical methods for thermal response** for both transpiration and ablation cooling. In order to design and dimensionate thermal protection systems, these developed models and tools require the input of **material data**. However, temperature management also depends on measurement and a **sensor network** provides health monitoring of ceramic heat shields. In order to validate the results from models, sensor measurement and the material characterization that supports both sensing and modelling, a **portable test cell for in-situ X-ray** was developed. It was first tested in a laboratory computed tomograph and then in a synchrotron facility.

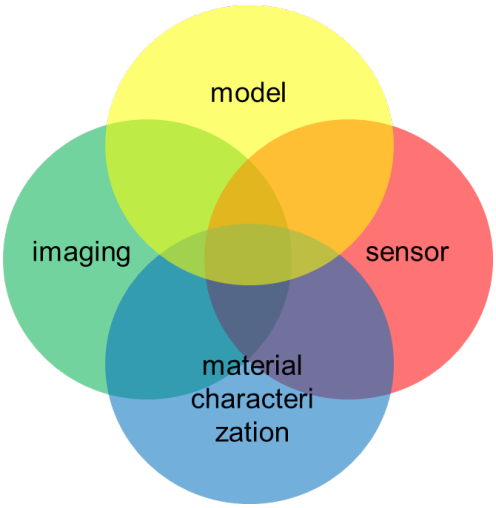

Fig. 1. Figure caption

2. Material

The purpose of a TPS is to protect a body from the severe heating encountered during hypersonic flight through a planetary atmosphere. Since TPS is a single point-of-failure subsystem, it is critical and its performance needs to be validated through ground test and analysis [1].

There are two classes of TPS. A reusable TPS has no change in its mass and thermophysical properties and is generally preferred at relatively mild, lower speed reentry and entry environments. The material choice for this type will be discussed below in C/C (when transpiration-cooled), C/C-SiC and Octra.

[1] *German Aerospace Center (DLR), Institute for Structures and Design, hannah.boehrk@dlr.de*
[2] *German Aerospace Center (DLR), Institute for Structures and Design*
[3] *Institute of Aerospace Thermodynamics, University Stuttgart*

The second class of TPS are ablators, mostly used for higher speed environments and can be categorized into: subliming, melting and vaporizing, and charring, depending on their phase change caused by the heat absorption. An in-house manufatured cork ablator is described and material values are givencbelow [1, 2].

2.1. C/C

In a first step, a green body of carbon fiber reinforced plastic (CFRP) is formed via autoclave, resin transfer moulding (RTM) or hot pressing techniques using commercially available 0°/90°C carbon fabrics impregnated with a phenolic resin. After curing, the green body is pyrolyzed in a second step at temperatures of up to 1650°C, which converts the phenolic matrix to amorphous carbon. Due to the volume shrinkage of the matrix and the geometrical stability of the C-fibre architecture, internal stresses are built up, leading to microcracks and a porous C/C preform.

2.2. C/C-SiC

In order to obtain C/C-SiC, the C/C material has to be siliconized by means of liquid silicon infiltration by capillary forces at T>1420°C. **Intrinsic electric material properties of C/C-SiC will be used within a health monitoring system and be given here [3]**.

To combine the permeability of C/C and the oxidation resistance of C/C-SiC, a new material development based on C/C-SiC fiber reinforced ceramics started at DLR Stuttgart [4]. Contrary to dense C/C-SiC materials, it has a porosity and permeability like C/C, which can be additionally adapted to the application purpose. Compared to C/C the oxidation resistance is significantly improved. Optimization of the material for transpiration cooling is carried out by selective insertion of cavities into the C/C by replacing fibers by non-stable fiber materials before pyrolysis. During pyrolysis, these fibers will be degraded forming a higher porosity. The material is named OCTRA. **The section will give an overview of the achieved material parameters [5]**.

2.3. Optimized Ceramic for Transpiration OCTRA

In order to profit from the permeability of C/C and the oxidation resistance of C/C-SiC, a new material development based on C/C-SiC fiber reinforced ceramics was started at DLR Stuttgart **[2]**. Contrary to dense C/C-SiC materials, it has a porosity and permeability like C/C, which can be adapted to the application purpose.

The optimization of the material is achieved through selective insertion of cavities into the pyrolized C/C material state . This is realized by replacing fibers by non-stable fiber materials before pyrolysis. During pyrolysis, these fibers are degraded forming a higher porosity.

The CFRP green body was made from 2D hybrid and carbon fabrics with a roving size of 3K using RTM technique, with the stacked fabrics infiltrated by a phenolic based resin. Furthermore, the hybrid fabric used was a mix of carbon and aramid fibers with a composition of 38.80% aramid fibers and 61.20% carbon fibers. The subsequent pyrolysis and silicon infiltration was conducted as described for the classic dense C/C-SiC process.

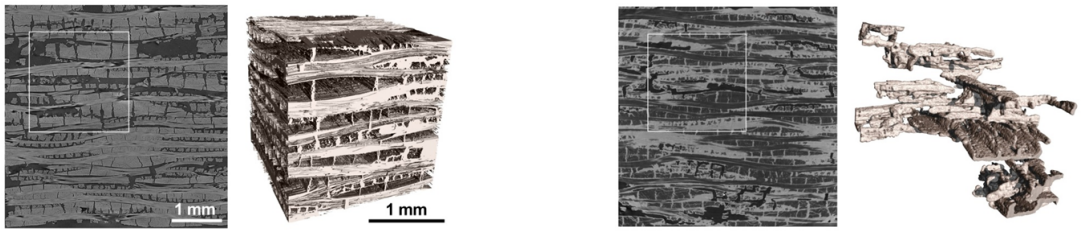

Fig. 2. X-ray CT image of the pore structure in the optimized ceramic C/C (left) and C/C-SiC (right) states

The microstructure of the CMC material manufactured by replacing non-stable fibers is presented in figure **??**. The figures show the interconnected pore structure of the optimized C/C caused by the limitation of matrix shrinkage due to the fiber reinforcement. **Figure 1 (right),** is a negative 3D image of the pore volume and it can be seen that this type of porosity is a channel type structure along the two fiber orientations. **...** pore volume which accounts for 30vol.% of the preform. Due to the decomposed aramid fiber the channel diameter increases up to 1mm.

In Figure 2 the pore structure after silicon infiltration is presented, which is reduced to 10vol.%. Partially, due to the formation of SiC and partially to residual Si trapped inside closed pores. The surface of the pore channels is much smoother than in the C/C state, caused by the SiC formation, which means the internal channel structure is entirely covered with SiC. The main orientation of these channel type structure remains along the fiber orientations. To assess the through-flow characteristics of the material, permeability and porosity are of fundamental importance. These parameters control the pressure loss over the porous material for a certain fluid mass flow, by means of porous injection or transpiration cooling, respectively. The different porosities e' and permeabilities, k_D and k_f, for the four OCTRA plates are given in Table 1. The Darcy coefficient k_D for OCTRA 40 is approximately 4 times as high as that for the less permeable OCTRA 20 material. In addition, Tab. 1 also provides the thermal properties of the materials. It can be seen that the thermal conductivity varies strongly depending on the fiber direction but the variation over the materials in contrast is very low. The density for a all materials is measured with 2.0$\pm$ 0.1 g/cm^3. Porosity was determined by the Archimedes method according to DIN 51918. Generally, the porosity increases with the sacrificial fiber volume fraction [5].

2.4. Phenolic Impregnated Cork Ablator

An in-house manufatured cork ablator is described and material values are given [1, 2]. To protect a launcher vehicle from thermal loads during the flight ascent phase the German Aerospace Center (DLR) in Stuttgart is developing a new cost-efficient thermal protection system (TPS). The investigations led to a sandwich structure design for the payload fairing based on a combination of GFRP layers, foam and a lightweight cork ablator material to meet requirements like high frequency (HF-) transparency.

The charring ablator normally provides the most efficient thermal-protection shield for the major portion of a manned entry vehicle [2]. Combining an ablator with the blunt body was an early breakthrough in TPS development and was first used in the Apollo era. This concept deflected, rejected, and reradiated the heat load instead of absorbing it [3]. An ablative TPS protects the vehicle via thermochemical phenomena including an ablation process, heat being consumed by a chemical reaction in the ablative material and leaving the vehicle as the material ablates away, and the creation of a char layer, which is an effective insulator and also effective at blocking radiated heat from the shock layer [4]. The physical principle of a charring ablation process is based on pyrolysis. The heat absorbed by the material provides the energy required for the material pyrolysis rather than being conducted further into the vehicle. This char layer acts as an insulator while the virgin material underneath continues to decompose and outgas. Pyrolysis gases, reaction and surface erosion products provide an additional insulation layer while being carried away from the high speed flow. In the present case, with a cork-based material, an additional swelling effect occurs due to internal pyrolysis gas products increasing pressure in the cork cells. A mechanical overview of an ablative TPS is illustrated in figure 1.

Preliminary tests of this phenolic resin based cork ablator are performed in order to get an assessment of its thermal capability. The material is tested in a radiation heated furnace to look for correlations between its density, compounding ratio and thermal characteristics. Thermal conductivity, degradation and the occurrence of swelling are studied under heat loads comparable to anticipated flight loads. The performed studies indicate promising results for a cost-efficient and well performing insulator for rocket flight ascent. Cork sheets in various densities were manufactured while using different resins and even the lowest-weight version demonstrates a reasonable thermal conductivity while being advantageous in shape flexibility.

For the presented material, cork granulate with a grain size of 0.5-1 mm and a density of 50-60 kg/m^3 is mixed either with liquid or dry phenolic resin and then hydraulically pressed whilst heated. The ablator

material for the performed tests is made from cork sheets of several densities, various compounding ratio and varying resins. Table 2 summarizes the used sheets with their properties altering in density, thickness, resin ratio and type.

Tabelle 1. Material properties of OCTRA and classic C/C-SiC materials [5]

	k_D [10^{-13} m^2]	k_f [10^{-9} m]	$\lambda_\parallel$ [W/mK]	$\lambda_\perp$ [W/mK]	c_p [J/kgK]	ρ [kg/m^3]	e' [%]
OCTRA 40	7.5±1.02	19±0.83	15.9–18.0	8.37–12.5	607–1020	2060	9.08
OCTRA 20	1.68±0.18	4.05±0.18	16.4–20.5	8.0–11.71	604–907	2010	7.44
C/C-SiC	–	–	17.0–22.6	7.5–10.3	690–1550	2300	-

Health Monitoring

Damage to thermal protection systems (TPS) during atmospheric re-entry is a severe safety issue, especially for reusable space transportation systems. There is a need for structural health monitoring systems and non-destructive inspection methods. The inherent electrical properties of carbon fiber reinforced material, e.g. silica carbide, will be used here for a health monitoring system of large structures based on electric impedance tomography in which the heat shield itself acts as the mass-efficient sensor. Heat load to reusable heat shields upon reentry is especially severe in stagnation point locations on vehicles.

Fig. 3. Test bench for time resolved resistance measurement

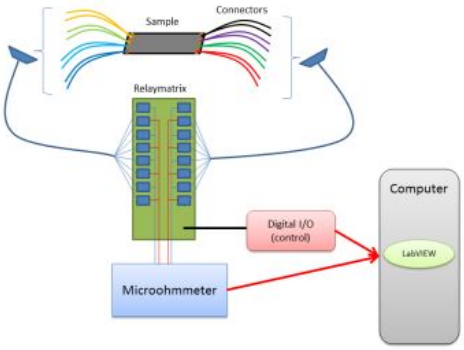

Fig. 4. measurement scheme

In this work electrical resistance measurements are used to detect damages in a TPS. This can be carried out in-situ. The change in resistance is an indicator for damage size and with use of post-processing algorithms the location of the damage can be determined. The details will be presented in a contribution by T Staebler (HiSST-2018_Abstr_1460891).

3. Transpiration Cooling

HEATS is a semi-analytical tool for the determination of transient material temperatures along a trajectory [1]. Therefore, it is used for preliminary design studies of thermal protection systems. In order to determine the transient wall heat flux to a material wall, HEATS solves the analytical equations for the oblique shock, and expansion fans are used to determine the state variables in the vicinity of the vehicle.

Moreover, the simulation of the porous structure including the internal coolant flow is also investigated in the simulation environment of the open source software OpenFOAM (Open source Field Operation and Manipulation) [6].

3.1. Cold iternal and outflow

Permeable fiber reinforced ceramics combine high temperature resistance of ceramics with excellent thermal shock behavior. However, due to the fiber reinforcement, they have anisotropic permeation characteristics. Here, investigations by **Gulli [8]** have shown that for complex porous structures the effective or local permeability varies along a contour. Combined with the problem at hand, where highest heat loads appear at regions with highest total pressure, it is necessary to **WAS?**. In order to do that, a porous carbon/carbon (C/C) cone was used as a reference experiment. A cone from porous C/C was machined from cylindrical samples out of a porous flat C/C plate, as shown on the left in Fig. 5. The plate in turn was laid up from stacked twill plies with fiber orientation of 0° and 90°.

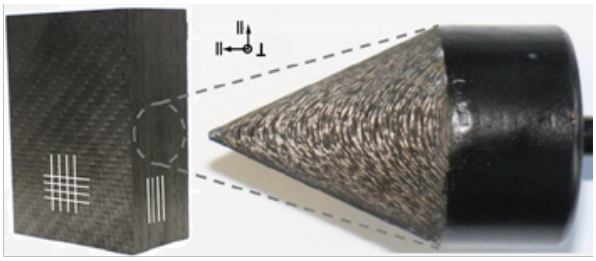

Fig. 5. C/C cone with fiber orientation.

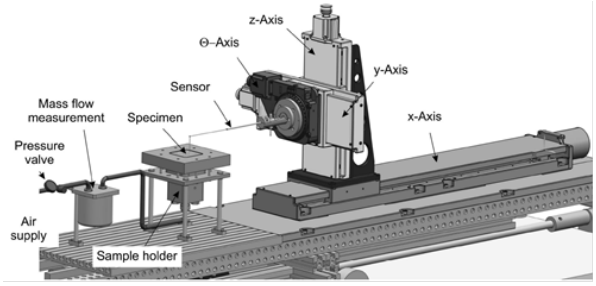

Fig. 6. Aorta test facility [7]

Measurements were carried out in the AORTA facility [9] shown in Fig. 6. A pitot sensor oriented perpendicular to the surface transverses in 2°-steps in horizontal steps along the flank of the cone, starting from the tip of the sample cone. Fig. 7 projects the results on cartesian coordinates when looking head-on the tip of the cone. The x- and y-direction in the graph depict the line along the flank of the cone from tip to base. It is obvious from this representation, that with the used material, a single measurement point is not representative. This is caused by the microscopic structure of the C/C. Here, in contrast to the idealized, homogeneous approach for a Darcy-flow, discrete, small channels determine the outflow characteristic. Moreover, Fig. 7 shows, that the outflow is concentrated around two angles (150° and 330°), representing the flow direction parallel to the plies of C/C. This was expected, since the permeability parallel to the plies is much higher compared to that of the perpendicular direction. Furthermore, the cone shows practically no flow at the tip region.

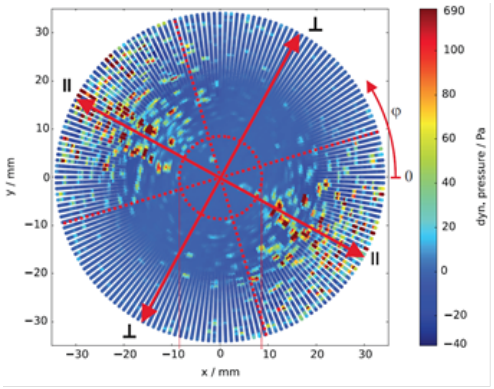

Fig. 7. Dynamic pressure results for 360° around the cone []

Additional measurements are performed under varying angle of the pitot probe with respect to the cone flank. The nomenclature of the angles is indicated in Fig. 8 where 90° corresponds to the probe facing perpendicularly onto the surface, i.e. the orientation in which all previous measurements were

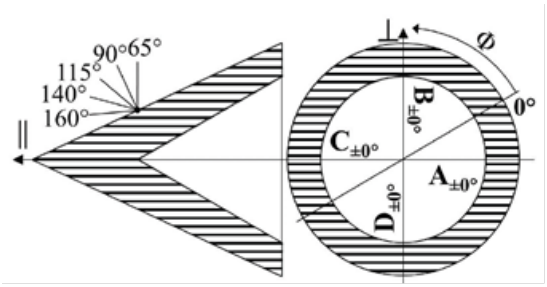

Fig. 8. Overview of measurement angles.

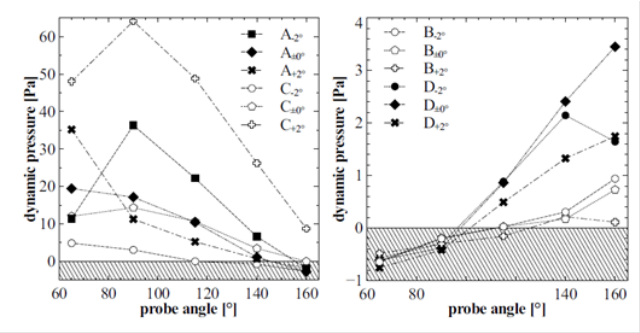

Fig. 9. Dynamic pressure measurement under varying pitot tube angles with respect to the sample surface flank. Left: At region with high permeability. Right: Results for the area with low permeability [8].

carried out. The results of these angular dependent measurements are shown in Fig. 18. The diagrams show the average dynamic pressure value along the surface versus the probe angle. It can be seen that the dynamic pressure changes over the surface angle. Negative dynamic pressures accounted to re-circulation from neighboring jets or possibly even induced by the pitot tube itself. While in regions A and C, where the fibers are oriented radially, all circumferential measurement series decrease after their maximum at 65° or 90° with increasing angle, the area of low permeability B and D, where the fiber orientation is tangential, the dynamic pressure increases with increasing pitot tube angle. This supports again the observation that the fiber orientation has a strong influence on the outflow direction.

Numericla analysis of the 3D coolant mass flow behavior, gives the contour plots in Fig. 10. They illustrate coolant pressure and area-specific mass flow distribution for the simulated experiment with a total coolant mass flow rate of 1 g/s. In the center figure, the coolant flow path in the same slice is illustrated by stream traces. The underlying color represents the Darcy velocity and indicates the low coolant flow velocities in the cylindrical part of the geometry. The stream traces in the top view of the right figure shows the curved coolant flow path leading to a diversion of large parts of the coolant mass flow rate towards the parallel fiber direction. This effect is based on the anisotropic permeability of the C/C material which is lower in the direction perpendicular to the fiber orientation

The strong effect of the material's anisotropy is also illustrated by the contour plots of the area-specific coolant mass flow given Fig. 11 which display an isometric and top view of the cone. Again, it is shown

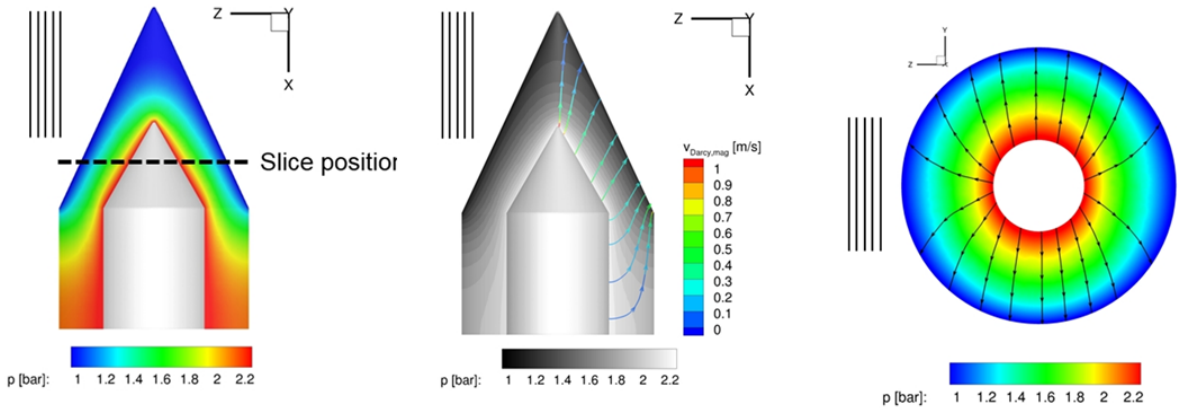

Fig. 10. Contour plot of coolant pressure in a slice through the porous cone. The material's carbon fiber direction is indicated by the stripes in the left top corner.

that more coolant gas is exiting the cone structure in areas with small alignment angles between radial coordinate and fiber axis. Furthermore, the plots illustrate the decrease of mass flow rate towards the cone tip with maximum values at the transition from cylindrical to conical part of the geometry. This is due to the increasing wall thickness (distance between plenum and cone surface) and consequently longer flow paths for coolant exiting in the tip region.

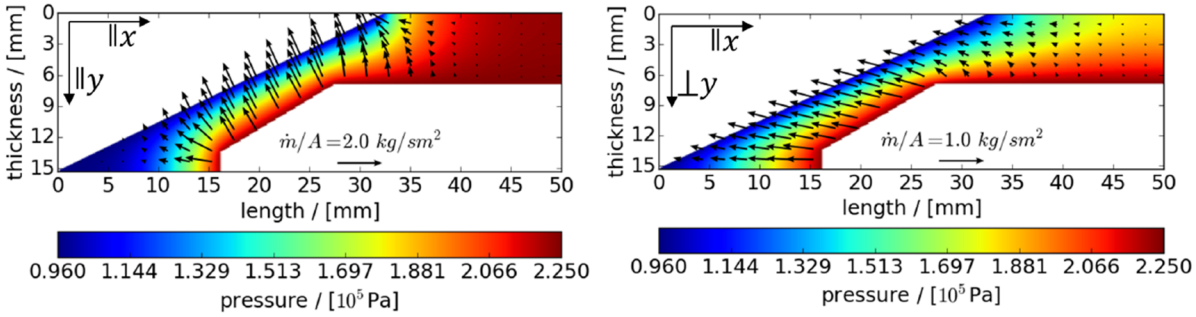

Fig. 11. Calculated two-dimensional pressure distributions for the cone.

3.2. Hot Flow Experiments

Two hot flow experiments are pursued. The first one is a duct flow at ITLR of Universität Stuttgart using permeable wall elements formed as flat plates or half wedges for fundamental studies on volumetric transpiration flows as given in the schematic of Fig. 12. All presented transpiration cooling experiments were performed in the ITLR hot gas facility under steady-state conditions at Ma=2.5, p_t=5 bar, T_t=500 K, and $\dot{m}_{hg}$≈0.436 kg/s. The rectangular test channel features a constant cross section of 35.4 mm height and 40 mm width. An overview of the facility and a cross sectional view of the modular channel setup are given in Figures 13 to 15. Further details will be presented in a contribution by D Prokein (HiSST 2018-0918).

As can be seen in Figure 13, the porous sample is mounted to the top channel wall with its surface flush to surrounding PEEK material, meant to insulate the ceramic sample from lateral thermal influence. The samples have been manufactured from C/C at DLR. For the present experiments the primary coolant flow direction is parallel to the ply orientation, i.e. parallel direction. A photograph of the reference sample including mounting frame with and without coolant plenum are given in Figures 14 and 15. The sampleitself is instrumented with ten internal thermocouples to determine the thermal state of the porous wall segment shown in Figure 3. Coolant mass flow rate, temperature and reservoir pressure are measured upstream of and inside the coolant plenum, respectively.

For the analysis of the sample surface and the wake region, the measurements of wall thermocouples are combined with infrared thermography. Figure 16 gives the temperature distribution over the channel length with air coolant. The symbols represent thermocouple measurements, whereas the curves are

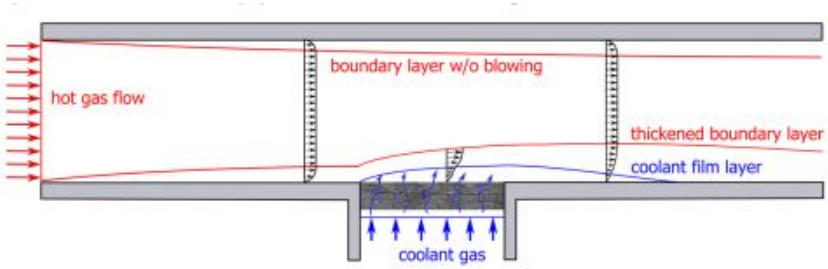

Fig. 12. Schematic of flow channel with transpiration-cooled wall segment.

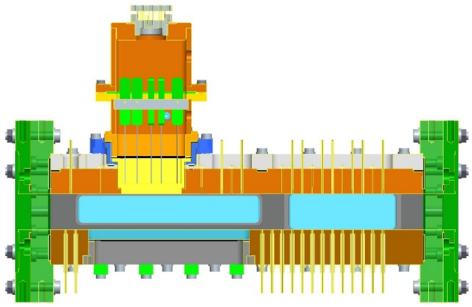

Fig. 13. Isometric and slice views of CAD model of new test section illustrating sample and coolant plenum integration as well as the optical accesses.

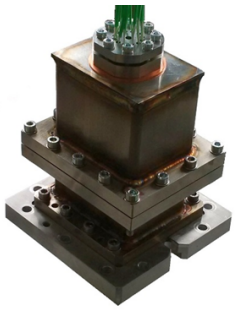

Fig. 14. Assembled coolant plenum ready to be attached to the test section. Porous sample is mounted at bottom side (covered).

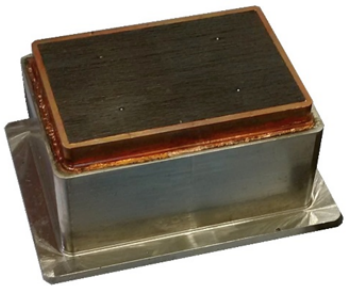

Fig. 15. Reference sample consisting of C/C structure with surrounding galvanised copper layer and stainless steel frame.

obtained by spanwise averaging of the corresponding in-situ calibrated infrared images. The symbol type represents different blowing parameters ranging from 0 to 0.75%. Figure 17 illustrates in situ calibrated IR images for air and helium injections varying from F=0.02% to F=0.75%. As the temperature distribution given in the IR plots facilitates the interpretation, we analyze and discuss both results together.

Figure 16 underlines the strong influence of transpiration cooling on the surface temperatures. Depending on the blowing ratio, the wall temperature drops significantly over the porous sample when compared to the values upstream of the sample. Although the temperatures rise again towards the end of the injection area and more drastically at the transition to the non-transpired wake region, a clear cooling effect remains visible for the complete length observed. Comparing the results for air and helium, a strong dependence on the coolant properties is found. Similar temperature levels can be reached by using considerable smaller mass flow rates of helium when compared to air. The superiority of helium as a coolant is due to the fluid's higher specific heat capacity which is roughly five times the value of air.

The IR temperature contour plots given in Fig. 17 support the previous findings and show a clear reduction of surface temperature on the transpired surface as well as in the wake region. An increased blowing ratio intensifies the cooling effect. Despite of the microscopic pores and their rather uniform distribution over the C/C surface, some inhomogeneities appear on the sample itself and in the wake

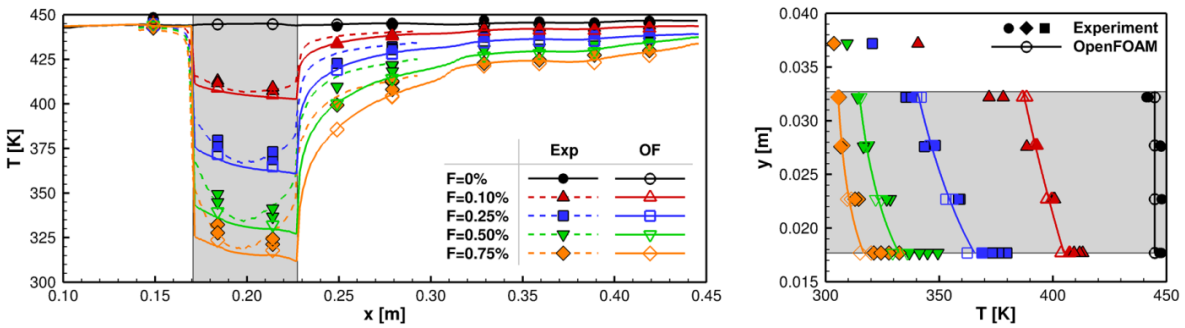

Fig. 16. Wall (left) and internal (right) temperatures for reference sample at different blowing ratios [Prokein:HiSST].

region, where a slight thermal stratification is notable. Comparing the illustrated cases of blowing with air and helium, similar infrared images are obtained for five times less helium mass flow rate. Examining the surface temperatures on sample and in the wake region more closely, it is interesting to note, that helium injection seems to have a weaker cooling effect on the sample surface whilst being more effective in the wake region. The observable differences become more prominent for higher blowing rates but remain small on the total scale. Possible explanations for this effect are currently reviewed.

For both coolants, we find a lateral contraction towards the sample center. While the higher temperatures in the leading-edge region can be explained by the coolant film build-up, the temperature increase at the sides and close to the sample's trailing edge may be due to different reasons. First, the so-called corner vortices which are characteristic for rectangular channel flows have an influence on the temperature levels close to the sidewall. Secondly, lateral heat conduction from the sample surroundings may cause a temperature increase. Both effects explain the slight differences between the continuous temperature distributions obtained through IR data (lines) and the thermocouple measurements (symbols) visible in Figure 16.

In order to quantify the effect of cooling, a cooling efficiency of the porous wall as proposed by Langener et al. [Langener:AIAAJ2011] can be calculated. The non-dimensional temperature ratio is defined by $\Theta=(T_{w0}-T)/(T_{w0}-T_C)$, where T_{w0} represents the uncooled wall temperature, T denotes the measured wall temperature for the considered blowing ratio and T_c is the coolant temperature at reservoir conditions. The four thermocouple readings at the surface determine the temperature T, whereas T_c is measured close to the sample surface within the coolant plenum. Figure **??** gives the cooling efficiency over blowing ratio for cooling with air, helium, argon, and CO2. The plenum temperature T_C is not constant but varies with blowing ratio and coolant gas used. Comparing the curves for the different coolant gases, we find a strong dependency of the cooling efficiency on the coolant's specific heat. Helium was found to be the most efficient coolant, followed by air and CO2 which exhibit similar results. Argon with the lowest specific heat shows the lowest efficiency of the four coolants tested. However, a strong temperature reduction and a high cooling efficiency up to around 90% is reached for all coolant gases when applying the respective maximum blowing ratios. Good agreement is found between all specific heat compensated curves (on the right) which indicates a linear correlation between cooling efficiency and specific heat capacity of the coolant. Following this, the cooling efficiency for the investigated case seems to be depending only on the coolant's capability to convey energy [Prokein:JPS2018].

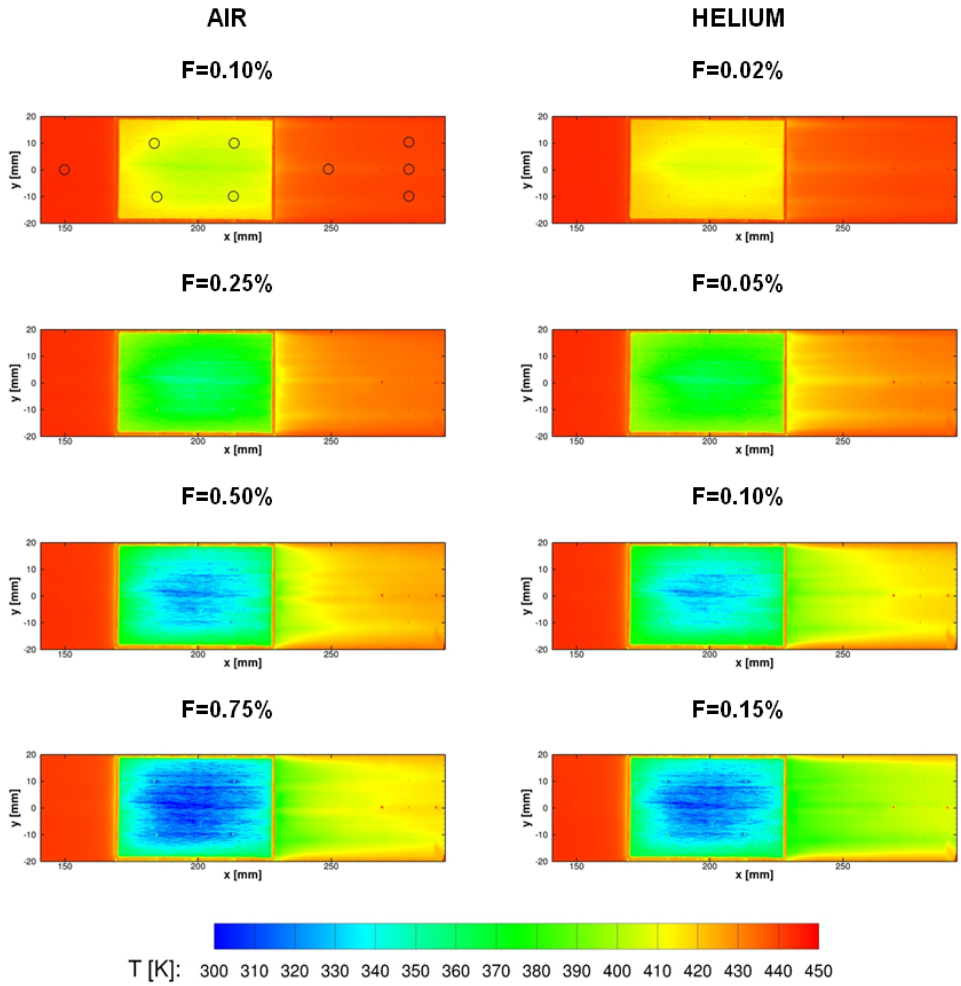

Fig. 17. Contour plots of wall temperature on sample surface and wake region obtained by means of in situ calibrated infrared thermography. The circles in the plot corresponding to F_{Air}=0.10% mark the positions of the thermocouples employed for the in-situ calibration (thermocouple tips and copper layer are not corrected for) [Prokein:JPC2018].

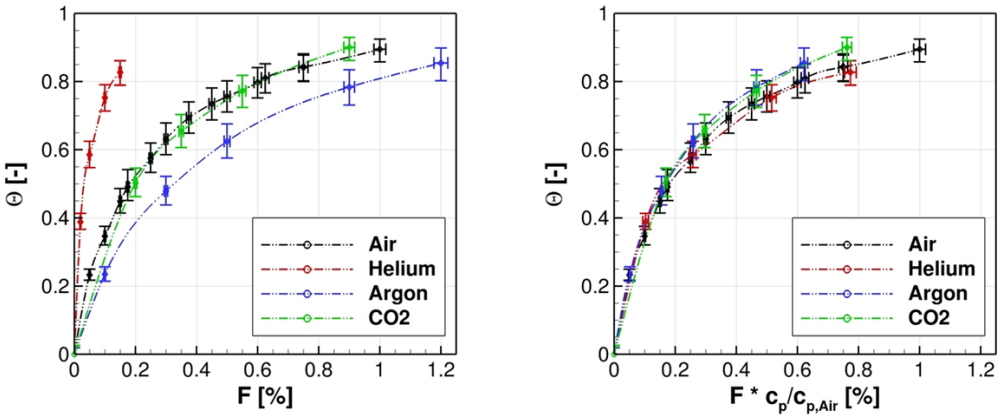

Fig. 18. Cooling efficiency for various gases of the porous wall over blowing ration (left) and specific heat capacity corrected blowing ratio (right) for various gas species [Prokein:JPC2018].

3.3. Functionally graded wedge structure

The second hot flow experiment is a wedge from functionally graded OCTRA material described above in a high enthalpy plasma jet at another university experiment at Institute of Space Systems (IRS). The details will be presented in a contribution by C Dittert (HiSST 2018-2280892).

In the design of the wedge, particular attention was paid to the outflow distribution across the surface, to ensure transpiration cooling up to the tip. Moreover, although only used in ground testing, the design presented here, is representative to a fully ceramic structure like a flight leading edge.

Here, a set of permeable material OCTRA 40 and OCTRA 20 was chosen, in order to provide the necessary cooling mass flow to the tip. The measured permeability for the OCTRA materials are shown in Tab. 1.

Fig.19 shows the ceramic wedge with its basic dimensions and the material selection. The opening angle of the wedge was 31.15°, this angle corresponds to the planned opening angle of the SHEFEX III vehicle tip [9]. All other dimensions were selected, such that the entire wedge remains within the plasma jet even at different angles of attack. The wedge itself is divided into three main parts, the tip (1) made of OCTRA 40, a center area (2) made of OCTRA 20 and dense C/C-SiC rear and side panels (3). Since the highest heat load will occur at the tip, this section needs to be cooled the most.

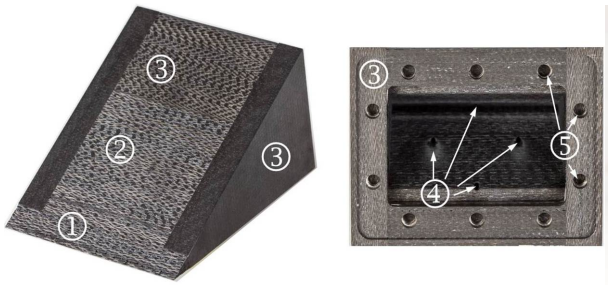

(1) OCTRA 40 (2) OCTRA 20
(3) dense C/C-SiC (4) thermocouple holes
(5) interface to sample holder

Fig. 19. C/C-SiC wedge

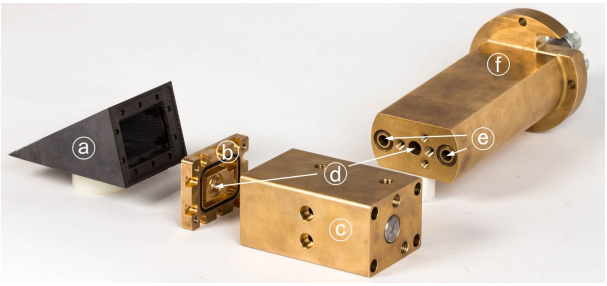

(a) wedge (b) wedge sealing plate
(c) sample holder adapter (d) cooling gas supply
(e) water cooling supply (f) sample base

Fig. 20. Explosion of the experimental setup

In addition to permeability, the outflow behavior can also adapted by the geometry of the part. However, since the external geometry is usually given, the adjustment must be made on the internal side. The inner opening angle is 22.0°, hence, the wall thickness is slightly increasing towards the rear. Along with the 2.5 mm thick and 7.5 mm deep notch at the tip and the permeability of the materials it is ensured, that the cooling gas is flowing in the direction of the highest heat load.

In order to attach the wedge to the sample holder, additional infrastructure is needed. In particular, gas supply in connection with the instrumentation of the thermocouples was challenging. Fig. 20 shows the interface parts used to connect the wedge into the plasma wind tunnel. The complete sample holder consists of three brass parts. The backplate of the wedge, labeled as (b), seals the reservoir of the wedge against the ambiance and connects the wedge to the sample holder. The remaining parts (c) and (f) are necessary in order to align the wedge in the direction of the plasma torch, with the possibility to adjust different angles of attack. The brass sample holder is water cooled with the in- and outlet lines marked with (e) in Fig.20. In addition to the water cooling line, the gas supply for the transpiration cooling (d) is included into the interface parts. Since the cooling gas has to be supplied all the way to the wedge, the instrumented thermocouples were routed into the wedge through the gas supply line.

In particular the ceramic C/C-SiC wedge is a unique, high temperature resistant part, which can be additionally cooled by transpiration cooling in order to expand the range of application even further.

4. In-Situ Imaging

In order to qualify and validate thermal protection materials (TPM) and their thermal response models, the materials have to be exposed to relevant testing environment of the hypersonic flow since the aero-thermochemistry plays an important role on the material efficiency. A portable furnace, which focuses on the radiative heating at sub-atmospheric pressure, was successfully used to image ablation processes in the industrial X-ray facility of DLR in 2015 [10]. It was the first time where the cork charring was experimentally monitored to be linear inside the material despite the externally observed volumetric swelling. To include the aerothermodynamic effects of the hypersonic flow, a new arcjet plasma furnace of portable size was designed and manufactured. Exposing the TPM to plasma flow allows us to study the effects of the convective heat flux (in addition to radiative) as well as diffusion in the boundary layer.

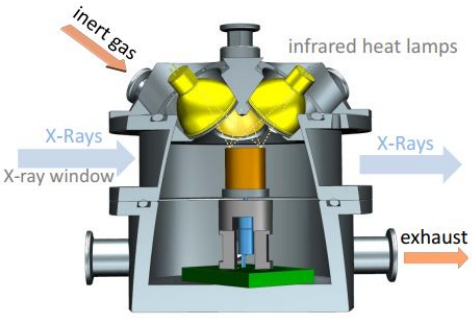

Fig. 21. Portable radiation furnace with sample and lamps.

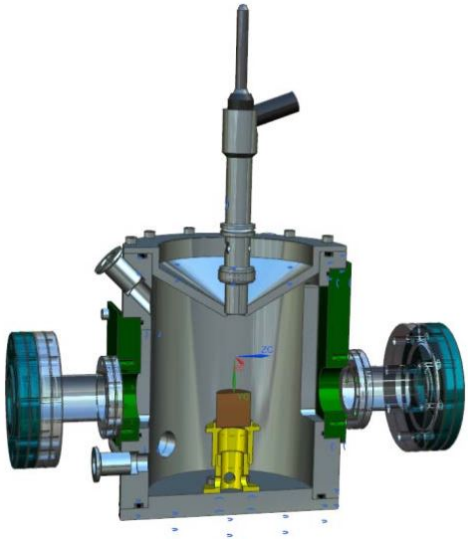

Fig. 22. Portable plasma furnace.

A challenge for performing the in-situ ablation measurements in an X-ray facility for 3D image reconstruction is the comparison of the time scales of ablation processes and the 2D radiograph acquisition rate. One must acquire a suffcient number of 2D images during 180 degree rotation to rebuild a high resolution 3D image. Therefore one must take into account the physical changes of the ablator sample when defining the acquisition rate. Another series of experiments was carried out in a synchrotron facility at KIT (Karlsruhe Instiute of Technology). Details on first results were presented in Sakraker et al. [Sakraker:Atlanta2018].

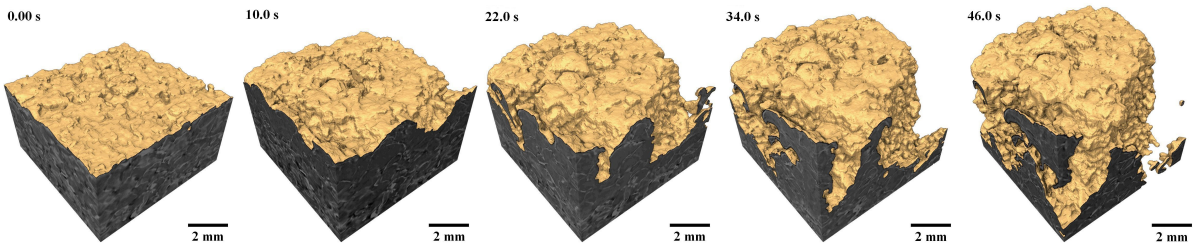

Fig. 23. Cork surface topology tracking from reconstructed 3D images

References

Literatur

[1] Böhrk, H. and Stokes, J., "Kinetic Parameters and Thermal Properties of a Cork-Based Material," *20th AIAA International Space Planes, Hypersonic Systems and Technologies Conference*, Glasgow, UK, Jul. 2015, AIAA 2015–3528.

[2] Mank, S. and Böhrk, H., "Preliminary Thermal Performance of a new cost efficient Phenolic Resin-based Cork Ablator for Rocket Ascent Protection," *8th European Workshop on Thermal Protection Systems and Hot Structures*, ESTEC, Noordwijk, The Netherlands, Apr. 2016.

[3] Stäbler, T., Böhrk, H. and Voggenreiter, H., "Characterisation of electrical resistance for CMC materials up to 2000 K," *Composites Part A: Applied Science and Manufacturing*, Vol. 112, 2018, pp. 25–31.

[4] Heidenreich, B., Hofmann, S., Jemmali, R., Frieß and Koch, D., "C/C-SiC Materials Based on Melt Infiltration - Manufacturing Methods and Experiences from Serial Production," *High Temperature Ceramic Matrix Composites 8*, edited by L. Zhang and D. Jiang, The American Ceramic Society, John Wiley and Sons, Hoboken, NJ, 2014, pp. 296 – 310.

[5] Dittert, C. and Kütemeyer, M., "Optimized Ceramic for Hypersonic Applications with Transpiration Cooling - OCTRA," *Global Forum on Advanced Materials and Technologies for Sustainable Development*, Toronto, Canada, Jul. 2016.

[6] Prokein, D., von Wolfersdorf, J. and Böhrk, H., "Analysis of Anisotropy Effects for Transpiration Cooled CMC Leading Edges using OpenFOAM," *20th AIAA International Space Planes, Hypersonic Systems and Technologies Conference*, Glasgow, UK, Jul. 2015, AIAA 2015–3552.

[7] Selzer, M., Hald, H., Schweikert, S. and Wolfersdorf, J., "Measurements of surface exhalation characteristics of porous fibre reinforced composites," *4th International Conference on Porous Media and its Applications in Science and Engineering*, Potsdam, Germany, Jun. 2012.

[8] Dittert, C., Selzer, M. and Böhrk, H., "Flow Field and Pressure Decay Analysis of Porous Cones," *AIAA Journal*, Vol. 55, No. 3, 2017, pp. 874–882.

[9] Dittert, C., Böhrk, H. and Weihs, H., "Wall Thickness Optimization of a Transpiration-Cooled Sharp Leading Edge at Atmospheric Re-Entry," *5th International Conference on Porous Media and Their Applications in Science, Engineering and Industry*, edited by K. Vafai. A. Bejan. A. Nakayama, and O. Manca, ECI Symposium Series, 2014.

[10] Böhrk, H. and Jemmali, R., "Time resolved quantitative imaging of charring in materials under temperatures above 1000 K," *Review of Scientific Instruments*, Vol. 87, No. 7, 2016, pp. 073701.